Radiotherapy and Oncology 136 (2019) 121–129

Contents lists available at ScienceDirect

Radiotherapy and Oncology

journal homepage: www.thegreenjournal.com

Original Article

Simultaneous acquisition of orthogonal plane cine imaging and isotropic 4D-MRI using super-resolution

Nikolai J. Mickevicius [a,*], Eric S. Paulson [a,b,c]

[a] Department of Radiation Oncology; [b] Department of Radiology; and [c] Department of Biophysics, Medical College of Wisconsin, Milwaukee, USA

ARTICLE INFO

Article history:
Received 24 May 2018
Received in revised form 30 March 2019
Accepted 3 April 2019
Available online 17 April 2019

Keywords:
MR-guided radiation therapy
Dose reconstruction
Intrafraction motion management
Truth in delivery analysis

ABSTRACT

Introduction: Effective management of intrafraction motion is critical to the success of MR-guided radiation therapy (MR-gRT) of abdominal or thoracic tumors. Recent developments have proposed the use of cine MRI to monitor motion and 4D-MRI to aid in the reconstruction of dose actually delivered to patients. The present work aims to develop and perform preliminary testing of an imaging framework capable of simultaneously acquiring orthogonal plane cine imaging and isotropic resolution 4D-MRI volumes using super-resolution methods.

Methods: A pulse sequence was developed to acquire time-locked cine imaging in sagittal and coronal planes while additionally acquiring 4D-MRIs in both planes simultaneously. Isotropic resolution 4D-MRIs were reconstructed by combining information from the orthogonal volumes using super-resolution methods. This method was tested in phantoms and in liver cancer patients.

Results: Simultaneous cine imaging in sagittal and coronal planes allowed monitoring of respiratory motion and an accurate binning of concurrently acquired 4D imaging slices into the appropriate respiratory phases. The super-resolution reconstruction methods improved the resolution of the 4D-MRI along both of the low-resolution slice-select dimensions.

Conclusions: The development and preliminary testing of an imaging framework capable of acquiring simultaneous orthogonal cine imaging and super-resolution 4D-MRI was performed. The promising results merit further investigation for use in dose reconstruction during MR-guided radiation therapy.

Recently, integrated MRI and radiotherapy treatment devices have been developed and are increasingly being introduced for clinical use [1–4]. These hybrid devices extend the advantages of MRI into the radiotherapy treatment room which, combined with sophisticated radiotherapy delivery systems, offer great potential to provide high-precision, personalized radiotherapy for patients [5].

With the ability to monitor the motion of targets and proximal organs at risk (OAR) in real time, using non-ionizing, high soft tissue contrast imaging, MR-guided radiotherapy (MR-gRT) permits highly conformal, hypofractionated RT in complex treatment sites such as the abdomen and thorax. Accurate reconstruction and accumulation of the actual dose deposited during RT is critical in order to correct for deviations between planned and delivered doses due to intrafraction motions arising from respiration, peristalsis, cardiac pulsations, organ filling, drifting, and bulk motion.

A number of approaches have been recently introduced to monitor intrafraction motion and reconstruct doses delivered within an MR-gRT fraction. One set of methods propose a real-time, 2D cine MRI-driven, principal component analysis (PCA)-based motion model that accommodates for deviations in the breathing pattern between a pre-beam 4D-MRI and throughout the treatment fraction [6,7]. This approach, however, is dependent on accurate deformable image registration (DIR) between the 2D and 4D volumes. Another recently proposed method, based on the principles of simultaneous orthogonal plane imaging (SOPI) [8], acquires 2D cine imaging necessary for real-time motion monitoring while simultaneously acquiring 4D-MRI in an imaging plane orthogonal to the 2D cine imaging [9]. A fixed navigator slice is used to sort the volumetric data into the appropriate respiratory phases [10]. With this technique, termed 4D-SOPI, serial 4D-MRI epochs can be reconstructed at intervals throughout the treatment fraction without relying on 2D-to-4D DIR, permitting reconstruction of dose delivered in the presence of respiration, organ filling, drifting, and bulk motions.

4D-SOPI combines in-plane and through-plane acceleration to maintain a fast frame rate while efficiently scanning slices in the 4D imaging plane. Due to g-factor [11] noise enhancements, these acceleration factors inhibit the acquisition of thin-slice isotropic resolution 4D-MRIs. An isotropic 4D-MRI may be desirable to min-

* Corresponding author at: 8701 W Watertown Plank Road, Milwaukee, WI 53221, USA.
E-mail address: nmickevicius@mcw.edu (N.J. Mickevicius).

https://doi.org/10.1016/j.radonc.2019.04.005
0167-8140/

imize registration errors when accumulating reconstructed dose. Furthermore, in the original implementation of 4D-SOPI, cine imaging was only performed in a single plane, or two parallel planes. To capture a pseudo-3D representation of dynamic targets during treatment, cine imaging in orthogonal planes (usually sagittal and coronal) has been proposed [6,8,12,13]. The SOPI method has the additional advantage that orthogonal cine slices are acquired in a time-locked fashion, which leads to improvements in motion estimation when compared with interleaved-slice cine imaging [14].

One way to address both of the issues with the original implementation of 4D-SOPI is to perform cine imaging in two planes while simultaneously acquiring 4D imaging slices in both planes. The thickness of the slices in each plane can be suitable to maintain a reasonable signal-to-noise ratio (SNR) after parallel imaging separation of the aliased slices. With the 4D-MRI volumes acquired in two planes, a super-resolution reconstruction can be applied to reconstruct isotropic resolution volumes at each respiratory phase without acquiring at a thin slice resolution. Many super-resolution (SR) methods exist for combining multiple low resolution (LR) datasets with different spatial information to create a high resolution dataset [15,16]. SR algorithms are applicable to 2D LR acquisitions with offset slice locations or multi-orientation LR acquisitions, not to 2D LR acquisitions acquired with shifted in-plane fields-of-view [17]. The SR volumes are typically reconstructed from multi-orientation LR volumes, making SR methods advantageous for combining orthogonal 4D-MRI datasets [18].

The present work explores the generation of SR 4D images using simultaneous orthogonal plane imaging (SR-4D-SOPI) for the simultaneous acquisition of prospective real-time orthogonal cine images and retrospective construction of serial, isotropic, 4D-MRI images. Preliminary testing of the SR-4D-SOPI acquisition and reconstruction framework is performed in a static phantom, dynamic phantom, and in patients.

Methods

Pulse sequence

The SR-4D-SOPI acquisition scheme and pulse sequence diagram are shown in Fig. 1. The equal echo-time (ETE) variant of SOPI is used in this study. Two consecutive multiband radiofrequency (RF) pulses excite a pair of slices in each of two orthogonal planes. Balancing of the zeroth gradient moments as described in Mickevicius et al (2017) [8] permits the simultaneous slice rewinding and phase encoding of slices along each axis prior to the echo time. A simultaneous image refocusing (SIR) [19] readout is utilized, and the receiver bandwidth is set to allow for the echo times of each slice group to be equal. One of the two slices excited along each axis remains fixed for cine imaging while the other slice along each axis dynamically changes position to acquire volumetric data. The key extension to the original SOPI method described here is the modulation of the imaging slice positions relative to the cine imaging slices. The pair of slices along each axis are excited in quadrature (i.e. with a 90° phase difference) [20] to minimize interference between their signals and to further encode the data. Multiband sinc RF pulses [21] are calculated on-the-fly since the RF pulse shape changes depending on the location of the imaging slice simultaneously acquired with the cine slice.

Data sorting

Information from the cine images is used to derive a 1D navigator to bin the imaging slices concurrently acquired with each cine frame. An image intensity projection is extracted from a sharp tissue boundary in every frame of the cine images. The center of mass of the image intensity along the projection was used as a 1D navigator for respiratory motion. The amplitude of the navigator was divided into equally sized bins with respect to the signal amplitude. Each imaging slice corresponding to each point in the naviga-

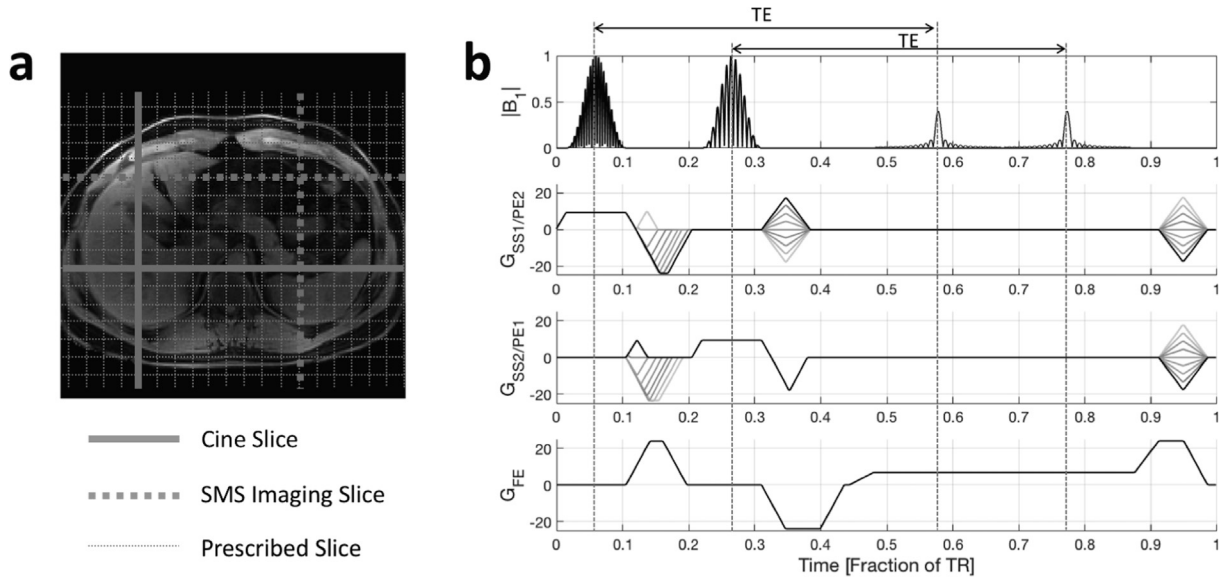

Fig. 1. (a) Super-resolution 4D-SOPI acquisition scheme. As indicated by the intersecting grid lines, two orthogonal stacks of slices (i.e. sagittal and coronal) are prescribed. Four slices are acquired in every frame (shown in bold). Within each orthogonal stack, a single navigator slice (solid bold) is acquired during every frame. The position of the imaging slices (dashed bold), which are acquired simultaneously with the navigator slices, changes from frame to frame. The imaging slices are retrospectively "binned" into respiratory phases based on the position of the anatomy within the navigator slices. (b) Super-resolution 4D-SOPI pulse sequence timing diagram. Two multiband RF pulses each excite two slices within each frame. Simultaneous image refocusing (SIR) and balancing of the zeroth gradient moment along the slice select (SS) and phase encoding (PE) directions allows the gradient echoes for each group of slices to be sampled under separate portions of the same readout period. See Mickevicius et al (2017) for information on calculating the gradient lobe areas for equal echo time (ETE) SOPI.

tor waveform was then sorted into the appropriate respiratory phase bin. If multiple slices in the same location exist within the same bin, the magnitude images were averaged. In the context of dose reconstruction for MR-gRT, a copy of the appropriate 4D imaging phase corresponding to each frame of the cine acquisition can be created and time-stamped according to the frame rate. This information, along with beam delivery logs and gradient nonlinearity distortion-corrected 4D-MRI volumes, can be used to reconstruct dose.

Super-resolution reconstruction

Two super-resolution algorithms were implemented and tested in this study. Both algorithms aim to solve the least squares problem posed in Eq. (1). SR reconstruction notation consistent with Plenge et al (2012) is subsequently used [16].

$$\boldsymbol{x} = \underset{\boldsymbol{x}}{argmin} \sum_{k=1}^{N} \| \boldsymbol{y}_k - \boldsymbol{A}_k \boldsymbol{x} \|_2^2 \tag{1}$$

Here, $\boldsymbol{x}$ is the SR volume data vector to be reconstructed, $\boldsymbol{y}$ is a vector of the acquired LR multislice 2D volumes. The index, k, counts through the LR volumes. In the present work, $N = 2$ for the sagittal and coronal volumes. The model, $\boldsymbol{A}$, is a matrix that maps the reconstructed isotropic data vector to the space of each acquired orthogonal volume. It includes a geometric transformation to match orientations and origins of the acquired LR orthogonal volumes ($\boldsymbol{G}$), blurring to model a Gaussian point spread function ($\boldsymbol{B}$), and a down-sampling and cropping operator ($\boldsymbol{D}$) (Eq. (2)). The matrix, $\boldsymbol{A}$, is represented as a sparse matrix in MATLAB (The MathWorks, Natick, MA) to conserve memory and reduce computation time.

$$\boldsymbol{A}_k = \boldsymbol{D}_k \boldsymbol{B}_k \boldsymbol{G}_k \tag{2}$$

The first algorithm tested is the iterative back-projection (IBP) method [22]. It begins with an initial guess and uses the difference between the forward propagation of the model and the acquired LR data to update the guess iteratively. The current implementation of IBP (Eq. (3)) is equivalent to the steepest descent method [23].

$$\boldsymbol{x}^{(i+1)} = \boldsymbol{x}^{(i)} + \sum_{k=1}^{N} \boldsymbol{A}_k^T \left(\boldsymbol{y}_k - \boldsymbol{A}_k \boldsymbol{x}^{(i)} \right) \tag{3}$$

Regularized least squares methods in SR reconstruction aim to better condition the inverse problem in Eq. (1). One such approach is to impose an ℓ_1 regularization penalty on the total variation (TV) of the volume in three dimensions. This method has been shown to promote a reduction in noise while minimizing blurring of edges [18]. The regularized problem is posed in Eq. (4).

$$\boldsymbol{x} = \underset{\boldsymbol{x}}{argmin} \sum_{k=1}^{N} \| \boldsymbol{y}_k - \boldsymbol{A}_k \boldsymbol{x} \|_2^2 + \lambda \| \boldsymbol{T} \boldsymbol{x} \|_1 \tag{4}$$

Here, T, represents the sparsifying TV transform, implemented as a finite difference in image intensity in three dimensions. The scalar regularization parameter, λ, allows for tradeoff between data consistency and the TV in the SR volume. This problem is solved via conjugate gradient (CG) methods, and this algorithm will be referred to by CG + TV for the remainder of this paper. For both algorithms, the SR reconstruction is initialized with the average of the LR sagittal and coronal volumes.

Experiments

The SR-4D-SOPI method was implemented on a Siemens 3T Verio (Siemens Healthineers, Erlangen, Germany) and tested in a structural phantom to assess resolution enhancements and in three liver cancer patients to validate the ability of SR reconstructions to work on retrospectively sorted respiratory phase volumes. A total of 21 coil elements (flexible anterior and built-in posterior arrays) were used for signal reception and for subsequent reconstruction. The research subjects consented to be a part of an Institutional Review Board approved study. Common imaging parameters for all scans include sagittal/coronal slice orientations, RF and gradient spoiling, flip angle of 10 degrees, TE/TR of 3.34/6.45 ms, matrix size of 128 × 128, and slice thickness of three times the in-plane resolution. For the phantom scan, a FOV of 340 × 340 mm, 42 sagittal slices, and 36 coronal slices were prescribed. For the *in vivo* scans, a FOV of 360 × 360 mm, 44 sagittal slices, and 36 coronal slices were prescribed. In each case the readout bandwidth was set to 765 Hz/pixel. An additional high-resolution (HR) scan of the phantom was acquired for comparison of the SR and LR volumes. A 3D isotropic RF-spoiled sequence with identical timing parameters as the SOPI scan was acquired at the in-plane resolution of the SOPI scans (2.66 mm). The mean structural similarity indices (SSIM) [24] of the SR and LR images were calculated relative to the HR images in the axial plane. The SSIM values were compared using a one-way ANOVA and, subsequently, Tukey's multiple comparisons test. A significance level of 0.05 was considered statistically significant.

The same acquisition as above was repeated in an MR-compatible 4D motion phantom (Model 008M, CIRS, Norfolk, MA). The phantom was programmed to move in the superior/inferior direction with a peak-to-peak amplitude of 20 mm, period of 5 s, and sine trajectory. The correlation coefficient of the surrogate signal, derived from the cine slices and the known trajectory, was calculated. Finally, the peak-to-peak displacement in the final super-resolution volumes between inspiration and expiration was calculated.

CAIPIRINHA RF phase cycling was used to impart a FOV/2 shift between slices excited along the same axis [25]. A brief calibration scan acquired low resolution data for calibration of 2D-SENSE-GRAPPA kernels used for un-aliasing along both the in-plane and through-plane dimensions [26]. The virtual conjugate coil (VCC) method was used to exploit phase differences between the SMS slices to further encode the data and reduce the g-factor [20]. The same RF pulse and RF phase tag were used to excite slices in the calibration and SR-4D-SOPI scans. It took approximately 1 second per pair of slices to calculate the 2D-SENSE-GRAPPA interpolation kernel weights. Additionally, an in-plane acceleration factor of three and 5/8 partial Fourier phase encoding sampling was used to improve the frame rate. A homodyne algorithm was implemented to restore the conjugate symmetric portions of k-space after the phase constrained 2D-SENSE-GRAPPA reconstruction [27]. A total of 48 phase encoding lines were acquired per frame, resulting in a sampling rate of 3.23 frames per second, with 4 slices being acquired per frame. It took 18.8 s and 19.3 s to acquire all prescribed un-sorted slices for the phantom and *in vivo* scans, respectively. The total duration of the 4D acquisition was approximately 6 min and 30 s. The application of the 2D-SENSE-GRAPPA kernel to each undersampled pair of slices took approximately 2 s in the current MATLAB implementation on an Apple MacBook Pro with a 4-core 2.8 GHz processor. The reconstruction time for an entire SR 4D dataset was approximately 80 min.

The patient imaging data were sorted into 6 sagittal and 6 coronal respiratory phases using the methods described above. For each respiratory phase and for the structural phantom data, a separate SR reconstruction was performed. The blurring operator was implemented as an anisotropic Gaussian filter with a 5 × 5 × 5 kernel. The standard deviation of the filter for the in-plane and through-plane dimensions are 0.25 and 1.28 pixels, respectively. These were chosen based on the point spread function considerations described in Van Reeth et al (2015) [18]. IBP and CG + TV

super-resolution reconstructions were performed with 80 and 10 iterations, respectively. The number of iterations was determined empirically. The regularization parameters, λ, were chosen empirically to be 1.0 and 0.12 times the median image intensity of the LR sagittal and coronal volumes for the phantom and *in vivo* experiments, respectively. Cubic interpolations of the LR volumes were also performed for comparison with the SR methods. All parallel imaging and super-resolution reconstructions were performed in MATLAB. Image intensity projections were plotted through sharp edges in both directions within the reformatted axial plane of all interpolated and super-resolution volumes to compare methods.

Results

The results of the super-resolution reconstruction from the sagittal/coronal phantom SOPI data are shown in Fig. 2. Compared with the cubic spline interpolation of the individual LR sagittal and LR coronal volumes, both the iterative back-projection and TV-regularized SR reconstructions offer resolution enhancements, as seen by the sharp edges in both directions within the axial plane. As expected, the ℓ_1 regularization penalty on TV was able to reduce the amount of noise in the SR images. The line profiles for the IBP and CG + TV SR algorithms show edges in the phantom within the axial plane equally as sharp, suggesting that the TV penalty is reducing noise without apparent loss of resolution. The line profiles for both algorithms match closely with the in-plane LR sagittal and LR coronal profiles. The mean SSIM of the SR, LR sagittal, and LR coronal images relative to the HR images in the axial plane were 0.8016, 0.7017, 0.7249, respectively. The one-way ANOVA analysis showed that the mean SSIM values between the SR, LR sagittal, and LR coronal volumes are significantly different ($p < 0.0001$). The mean SSIM values between SR and LR sagittal and LR coronal, individually, were significantly different ($p < 0.0001$).

Example sagittal and coronal images from a single frame of the *in vivo* experiment are shown in the top of Fig. 3 for subject 1. Small amounts of noise enhancement can be seen due to g-factor penalties from the highly accelerated acquisition. Additionally, a small amount of residual aliasing after the parallel imaging reconstruction can be seen on the patient's left side of the coronal image, as indicated by the white arrow. The residual aliasing artifact manifests as a subtle overlay of the fat signal from the outer edge of the first subject's right side. The bottom of Fig. 3 depicts the 1D motion surrogate signal derived from the cine imaging time series. This waveform was used to sort the concurrently acquired imaging slices into the appropriate respiratory phase.

Cubic interpolation and SR reconstructions of the respiratory phase at end expiration are displayed in Fig. 4. Similar to the phantom reconstructions, both the IBP and CG + TV SR algorithms were able to reconstruct isotropic resolution volumes from the LR sagittal and LR coronal acquisitions. In order to achieve similar levels of noise reduction with the CG + TV algorithm as observed in the phantom dataset, a more significant blurring occurred. The *in vivo* CG + TV images still provide sufficient resolution to define structures better than either of the individual LR reformatted volumes, but the images are not as sharp as those from the IBP algorithm.

Images in three planes are shown for the IBP and CG + TV algorithms for all six respiratory phases in Figs. 5 and 6, respectively. The white lines on the sagittal and coronal images provide a reference to visualize how the moving anatomy is resolved by the retrospective sorting of the SOPI images. Respiratory motion is nicely resolved without any mismatching of sorted slices propagating through the super-resolution reconstructions.

The motion surrogate derived from the cine images during the dynamic phantom experiment was highly correlated with the actual motion used to drive the phantom ($R = 0.9904$). The peak-to-peak displacement of the target (i.e. between inspiration and expiration) was found to be precisely 20 mm as expected for both the IBP and CG + TV SR reconstructions. The peak-to-peak motion in the superior/inferior dimension for subjects 1–3 was measured

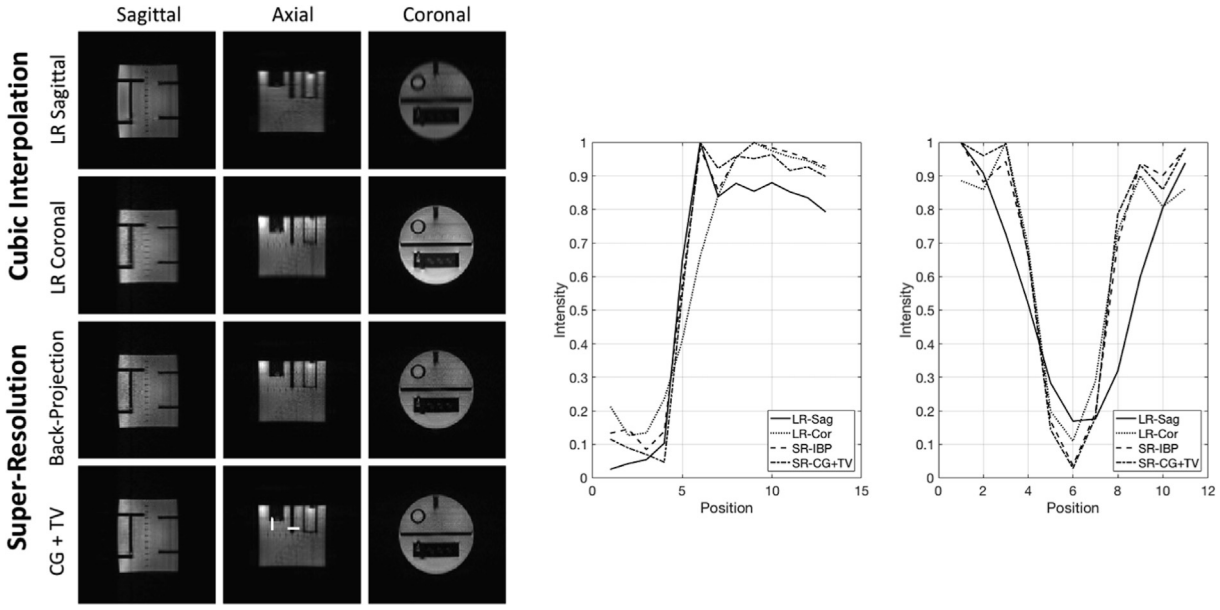

Fig. 2. (Left) Phantom experiment results. The low-resolution (LR) sagittal and coronal acquisitions are shown in the top two rows. The images were resampled to the isotropic resolution using cubic interpolation. The bottom two rows display back-projection and total variation-regularized super-resolution reconstructions from the LR sagittal and LR coronal acquisition. (Right) Intensity projections for all phantom reconstructions through line profiles drawn on the CG + TV reconstruction on the left of the figure. The super-resolution algorithms provide sharp edges in each direction within the axial plane compared to the interpolated volumes which are markedly blurry. The blurring introduced with the TV penalty is minimal compared to the IBP algorithm for this phantom dataset.

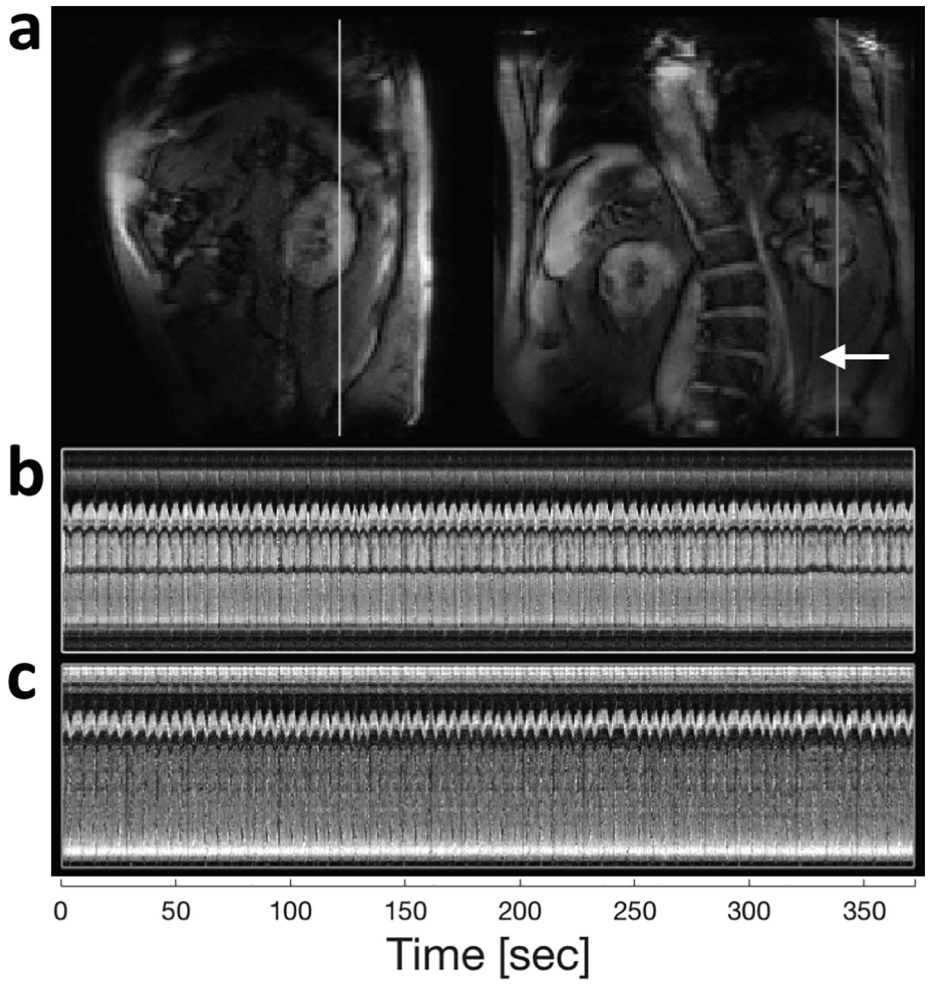

Fig. 3. (a) Simultaneously acquired sagittal and coronal navigator slices from a single frame of the SR-4D-SOPI acquisition in a liver patient. The white arrow indicates incomplete unaliasing from the parallel imaging algorithm. (b,c) Image intensity projections plotted over time for the sagittal and coronal cine slices, respectively.

to be 13.28, 15.94, and 10.62 mm, respectively, from the cine imaging data. The peak-to-peak motion measured from the binned SR reconstructions matched those made from the cine imaging data.

Discussion

A novel approach was presented that permits the simultaneous acquisition of cine and 4D-MRI imaging in two orthogonal planes. The cine imaging data serve two purposes. First, they can be used for prospective, real-time, intrafraction motion management during MR-gRT. Second, they are used to retrospectively sort the concurrently acquired 4D-MRI slices into appropriate respiratory phase bins. The simultaneous acquisition of multi-respiratory phase 3D volumes enables retrospective, super-resolution reconstructions of isotropic 4D-MRI epochs.

The iterative back-projection and the ℓ_1-regularized total variation super-resolution algorithms tested in this work both were able to reconstruct isotropic resolution volumes from two simultaneously acquired sagittal and coronal 4D-MRIs. The CG + TV algorithm, with its penalty on the total variation in the volume, reduced the noise in the SR images compared with the IBP algorithm at the expense of slight loss in resolution. The blurring introduced with the CG + TV method was more prominent in the *in vivo* 4D MRI versus the static reconstruction of the structural phantom. This may be due to slight misalignments between sorted slices within each bin from the dynamic *in vivo* acquisition. The TV penalty may be averaging out the misalignments causing blurring. In addition to providing sharper images, the IBP algorithm does not require the extra step of determining the appropriate scalar regularization parameter to provide the optimal tradeoff between noise and image sharpness. Both algorithms yielded motion estimates consistent with those expected from a controlled dynamic motion phantom experiment.

The distance between simultaneously excited slices varies throughout the course of the acquisition. For some slices, the center-to-center distance between SMS slices can be only the nominal slice thickness. The low time-bandwidth product RF pulses employed in this work caused some interference when slices are spaced so closely together. However, the artifacts produced due to this effect appear to be rather benign. CAIPIRINHA RF phase cycling was used to achieve a FOV/2 shift between the SMS slices excited along each axis. This achieved a reasonable SNR with such closely spaced slices. Further optimization can determine the appropriate slice shift to maximize SNR for each pair of SMS slices individually [28].

The relatively thick slices used in the LR sagittal and coronal 4D-SOPI acquisition cause partial saturation bands to propagate into the super-resolution reconstructions. These bands are not expected to affect image registrations of the SR-4D-MRI epochs, based on prior work in which each phase of a LR 4D-SOPI volume with one saturation band was successfully registered to a reference

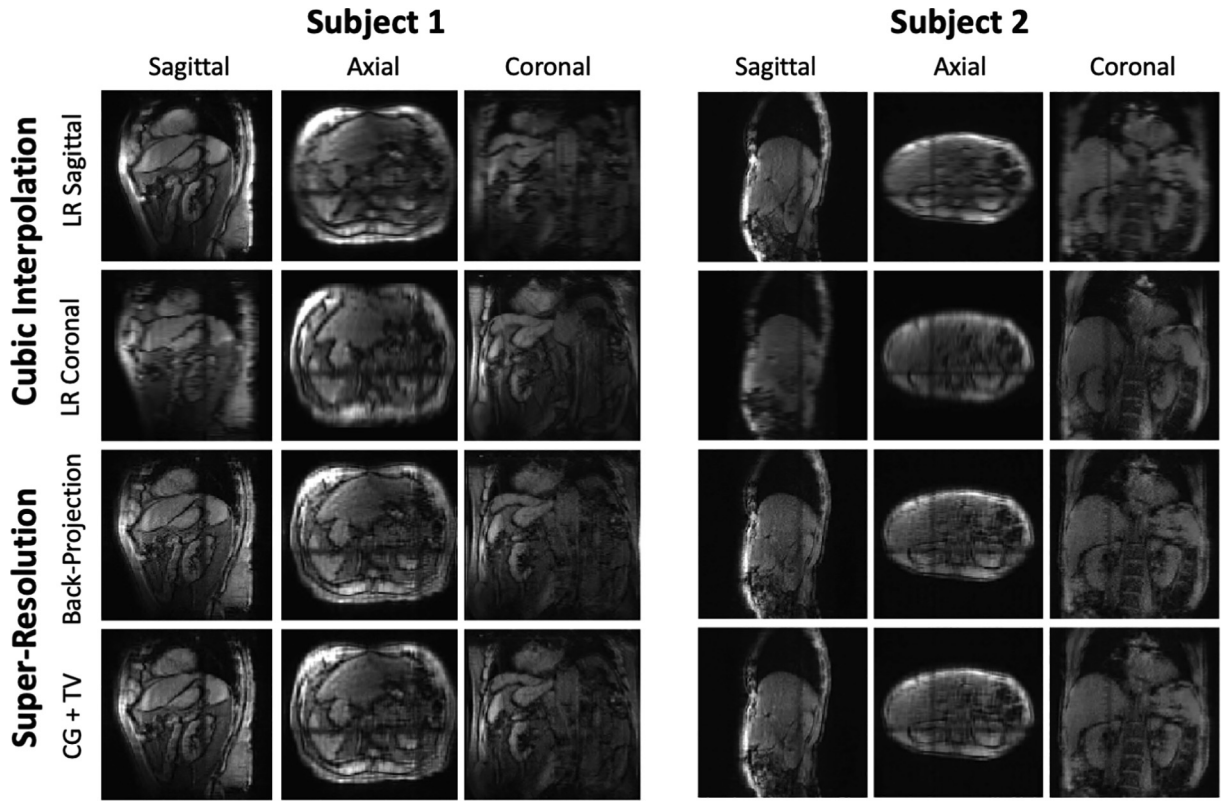

Fig. 4. In vivo reconstructions for the end-expiratory respiratory phase. Cubic spline interpolations of the low-resolution sagittal and coronal acquisitions are shown in the top two rows. The back-projection and TV-regularized super-resolution reconstructions are shown in the bottom two rows. Improvement in resolution is visually apparent by the sharper edges in the SR reconstructions in both directions within the axial plane relative to the cubic spline interpolated datasets.

phase to accumulate reconstructed doses [9]. Additionally, it has been previously shown that robust target tracking in 3D is possible with SOPI despite the saturation bands [8].

Large fields of view are necessary to achieve appropriate volumetric slice coverage without aliasing along the phase encoding direction. Coupled with a relatively small matrix size (128×128), the resulting super-resolution volumes are between 2.5 mm and 2.9 mm isotropic. These resolutions are one the order of typical grid sizes employed for radiation dose calculations. However, a finer resolution may be desired if more accurate delineations are to be made. In this case, higher acceleration factors will be required to maintain a frame rate reasonable for motion monitoring while improving resolution. The use of deep convolutional neural networks to aid in the reconstruction of highly accelerated images can be investigated [29].

In the current implementation of SR-4D-SOPI, a single navigator slice and a single imaging slice are acquired simultaneously in each plane. Even with the acceleration factors employed in this work, small amounts of residual aliasing were observed in the images reconstructed with the phase-constrained 2D-SENSE-GRAPPA algorithm. If higher density phased-array coils were used for signal reception, these artifacts would be reduced, and the through-plane acceleration factor could perceivably be increased to three simultaneous slices per axis. This would provide additional flexibility to tailor the acquisition to the particular target type. For example, MR-gRT of the pancreas may benefit from real-time motion monitoring of the pancreas and the duodenum. Adding additional cine slices intersecting the lung-liver interface would allow the navigator information to be obtained in addition to the real-time motion monitoring of the targets and OAR. This will be kept in consideration for future implementations on scanners with more favorable receive coil geometries.

The two stationary orthogonal navigator slices resulted in reduced efficiency of reconstructing 4D-MRI in SR-4D-SOPI compared to the original 4D-SOPI implementation. Only a single 4D-MRI volume was reconstructed from the 6.5 min of scan data in the present work compared to three unique 4D-MRI epochs from 7.5 min of scan data in the original implementation [8]. The trade-offs between efficiency of reconstructing 4D-MRI (and therefore the number of 4D-MRI epochs) and need for 4D-MRI with isotropic resolution for dose reconstruction and accumulation will be the focus of future work.

The robustness of the SR-4D-SOPI method was not extensively examined. While the patients in this study were not coached to breathe consistently, their respiratory motion patterns were fairly consistent. An amplitude-based sorting of the data into respiratory bins was selected for its robustness to inconsistencies in end-inspiratory position. More in-depth studies will need to investigate differences in SR-4D-SOPI reconstructions for different sorting algorithms. Furthermore, there is a large dependence on favorable coil geometry for performing the parallel imaging-based separation of slices and in-plane k-space interpolation. Without the use of advanced, deep learning-based image reconstruction methods [29,30], translation of this method onto hybrid MR/RT systems with limited RF coil channels may be challenging.

The overall image quality of the SR-4D-SOPI volumes is comparable to that achieved using non-SR 4D-SOPI with thinner slices [31]. The diagnostic image quality of the 4D volumes derived from high-resolution 3D stack-of-stars sequences is superior to that achieved with SR-4D-SOPI. However, the SR-4D-SOPI has the advantage of simultaneously acquiring 2D cine imaging in multiple planes while simultaneously providing 4D images. The contrast achievable with SOPI methods is not as flexible as other 4D-MRI methods since gradient spoiling is required. Therefore, it is limited

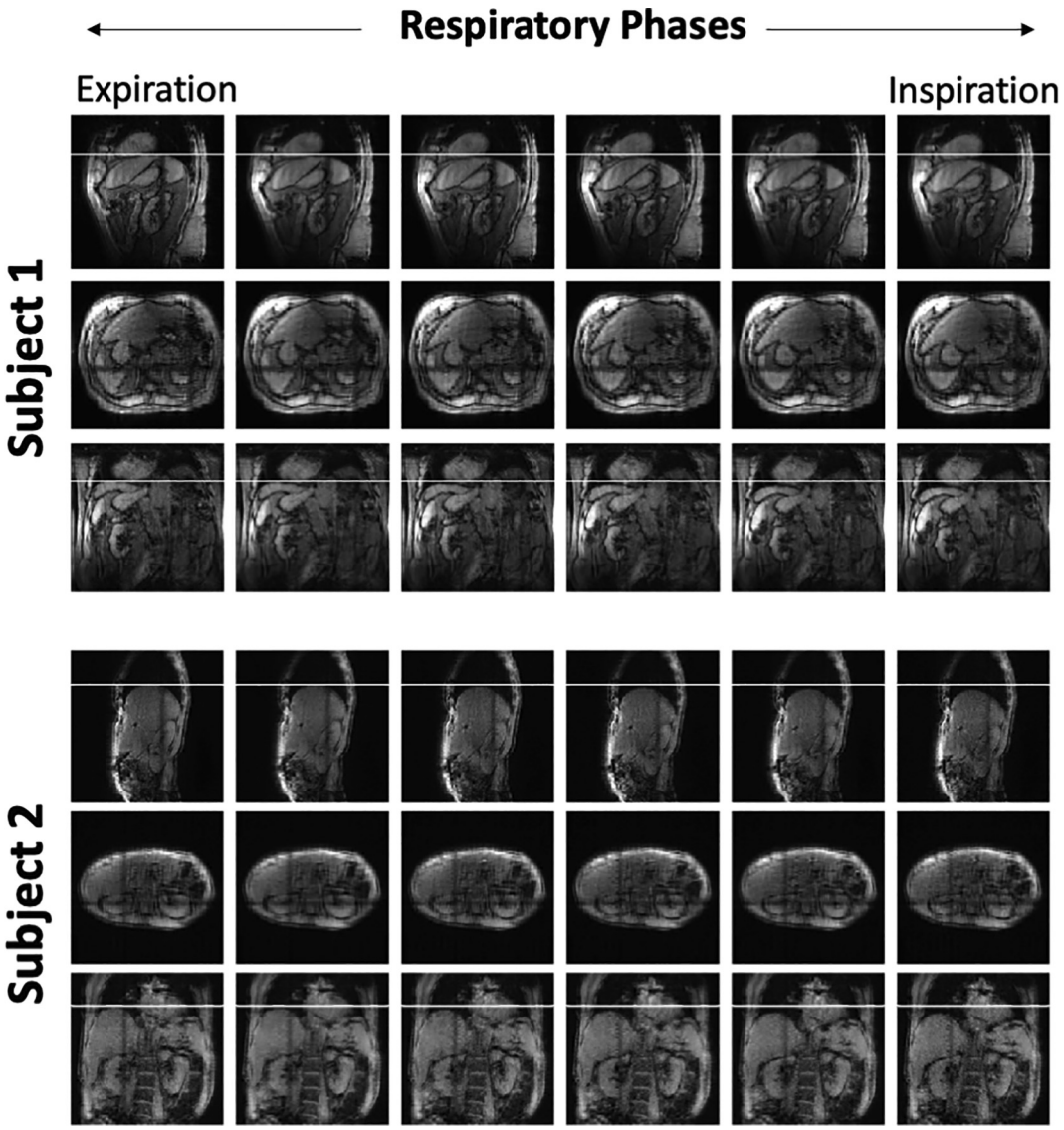

Fig. 5. In vivo IBP super-resolution reconstructions across six respiratory phase bins. The white reference lines on the sagittal and coronal images mark anatomical positions at the end of expiration, facilitating visualization of the difference in the position between respiratory phase bins.

to T1-weighted using RF-spoiling, or low SNR T2-weighting using a time-reversed gradient-spoiled sequence.

In the present study, each SR reconstruction was performed for each respiratory phase individually. If a sufficient number of respiratory phases are reconstructed, the motion between phases may be assumed to be slowly varying. Thus extending the SR reconstruction to 4D instead of 3D and employing the TV penalty along the respiratory phase dimension may help improve image quality. The TV penalty has been used along the temporal dimension for reconstructing multi-phase 3D volumes from retrospectively sorted radial stack-of-stars acquisitions [32] and has been shown to be a robust 4D-MRI method [33–35]. The TV constraint along the respiratory dimension may also allow the lowering or elimination of the regularization parameter imposing TV constraints on the x, y, and z dimensions, resulting in better within-volume resolution.

Other recent developments using super-resolution to improve 4D-MRI have been recently presented. While the SR reconstruction methods employed in this work were most similar to Van Reeth et al (2015) [18], there is potential for the images presented here to be improved through the use DIR-based super-resolution 4D-MRI methods such as those presented in Li et al. (2017) [36] and Freedman et al. (2018) [37]. However, the main advantage of 4D-SOPI is that DIR is not required to reconstruct 4D-MRI volumes for dose reconstruction. Accumulation of reconstructed doses to a reference phase, however, would still require DIR.

The future use of the SR-4D-SOPI method for dose reconstruction in MR-gRT will require a few key developments. First, a real-time implementation of the 2D-SENSE-GRAPPA reconstruction algorithm is needed on MR-gRT systems (or real-time deep learning reconstructions for MR-gRT systems with limited receive coil channels, as discussed previously). Second, accurate and efficient tools that automate recalculation of dose on each 4D-MRI phase and accumulate the dose to a reference volume are required.

The SR-4D-SOPI method was demonstrated to provide cine imaging in two orthogonal planes while simultaneously providing low-resolution 4D-MRI in the same two orthogonal planes. A super-resolution reconstruction was able to successfully combine the two LR 4D-MRI datasets into one isotropic resolution 4D-MRI. In the future, this preliminary evaluation of the technical

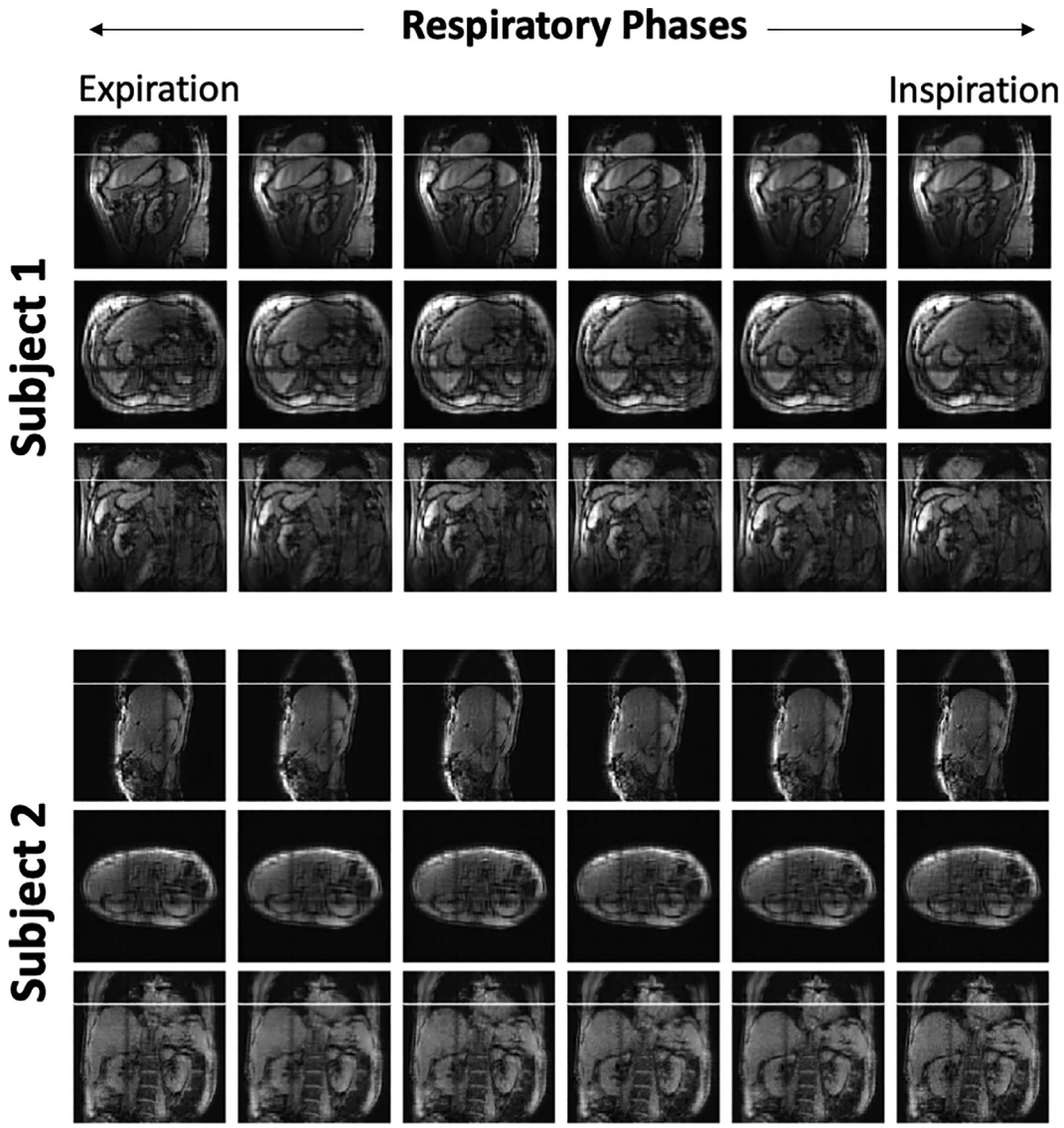

Fig. 6. In vivo CG + TV super-resolution reconstructions across all six respiratory phase bins. The white reference lines on the sagittal and coronal images mark anatomical positions at the end of expiration, facilitating visualization of the difference in the position between respiratory phase bins.

feasibility of SR-4D-SOPI will undergo a rigorous clinical evaluation in the context of motion monitoring and dose reconstruction for MR-gRT.

Conflicts of interest

None.

References

[1] Lagendijk JJW, Raaymakers BW, van Vulpen M. The magnetic resonance imaging-linac system. Semin Radiat Oncol 2014;24:207–9. https://doi.org/10.1016/j.semradonc.2014.02.009.

[2] Mutic S, Dempsey JF. The ViewRay system: magnetic resonance-guided and controlled radiotherapy. Semin Radiat Oncol 2014;24:196–9. https://doi.org/10.1016/j.semradonc.2014.02.008.

[3] Keall PJ, Barton M, Crozier S. The Australian magnetic resonance imaging-linac program. Semin Radiat Oncol 2014;24:203–6. https://doi.org/10.1016/j.semradonc.2014.02.015.

[4] Fallone BG. The rotating biplanar linac-magnetic resonance imaging system. Semin Radiat Oncol 2014;24:200–2. https://doi.org/10.1016/j.semradonc.2014.02.011.

[5] Kupelian P, Sonke J. Magnetic resonance – guided adaptive radiotherapy: a solution to the future. Semin Radiat Oncol 2014;24:227–32. https://doi.org/10.1016/j.semradonc.2014.02.013.

[6] Stemkens B, Tijssen RHN, de Senneville BD, Lagendijk JJW, van den Berg CAT. Image-driven, model-based 3D abdominal motion estimation for MR-guided radiotherapy. Phys Med Biol 2016;61:5335–55. https://doi.org/10.1088/0031-9155/61/14/5335.

[7] Harris W, Yin FF, Wang C, Zhang Y, Cai J, Ren L. Accelerating volumetric cine MRI (VC-MRI) using undersampling for real-time 3D target localization/tracking in radiation therapy: a feasibility study. Phys Med Biol 2018;63. https://doi.org/10.1088/1361-6560/aa9746.

[8] Mickevicius NJ, Paulson ES. Simultaneous orthogonal plane imaging. Magn Reson Med 2017;78:1700–10. https://doi.org/10.1002/mrm.26555.

[9] Mickevicius NJ, Chen X, Boyd Z, Lee HJ, Ibbott GS, Paulson ES. Novel simultaneous motion monitoring and truth in delivery analysis framework for MR-guided radiotherapy. Proc Am Assoc Phys Med 2018.

[10] von Siebenthal M, Szekely G, Gamper U, Boesiger P, Lomax A, Cattin P. 4D MR imaging of respiratory organ motion and its variability. Phys Med Biol 2007;52:1547–64. https://doi.org/10.1088/0031-9155/52/6/001.

[11] Pruessmann KP, Weiger M, Scheidegger MB, Boesiger P. SENSE: sensitivity encoding for fast MRI. Magn Reson Med 1999;42:952–62.

[12] Preiswerk F, Toews M, Cheng C-C, Chiou JG, Mei C-S, Schaefer LF, et al. Hybrid MRI ultrasound acquisitions, and scannerless real-time imaging. Magn Reson Med 2016. https://doi.org/10.1002/mrm.26467.

[13] Tryggestad E, Flammang A, Hales R, Herman J, Lee J, McNutt T, et al. 4D tumor centroid tracking using orthogonal 2D dynamic MRI: implications for radiotherapy planning. Med Phys 2013;40:. https://doi.org/10.1118/1.4818656091712.

[14] Mickevicius NJ, Paulson ES. Simultaneous orthogonal plane cine imaging with balanced steady-state free-precession contrast using k-t GRAPPA. Phys Med Biol 2018. https://doi.org/10.1088/1361-6560/aad008.

[15] Van Reeth E, Tham IWK, Tan CH, Poh CL. Super-resolution in magnetic resonance imaging: a review. Concepts Magn Reson Part A 2012;40A:306–25. https://doi.org/10.1002/cmr.a.21249.
[16] Plenge E, Poot DHJ, Bernsen M, Kotek G, Houston G, Wielopolski P, et al. Super-resolution methods in MRI: can they improve the trade-off between resolution, signal-to-noise ratio, and acquisition time? Magn Reson Med 2012;68:1983–93. https://doi.org/10.1002/mrm.24187.
[17] Scheffler K. Superresolution in MRI? Magn Reson Med 2002;48:408. https://doi.org/10.1002/mrm.10203.
[18] Van Reeth E, Tan CH, Tham IW, Poh CL. Isotropic reconstruction of a 4-D MRI thoracic sequence using super-resolution. Magn Reson Med 2015;73:784–93. https://doi.org/10.1002/mrm.25157.
[19] Feinberg DA, Reese TG, Wedeen VJ. Simultaneous echo refocusing in EPI. Magn Reson Med 2002;48:1–5. https://doi.org/10.1002/mrm.10227.
[20] Blaimer M, Choli M, Jakob PM, Griswold MA, Breuer FA. Multiband phase-constrained parallel MRI. Magn Reson Med 2013;69:974–80. https://doi.org/10.1002/mrm.24685.
[21] Souza SP, Szumowski J, Dumoulin CL, Plewes DP, Glover G. SIMA: simultaneous multislice acquisition of MR images by Hadamard-encoded excitation. J Comput Assist Tomogr 1988;12:1026–30.
[22] Irani M, Peleg S. Improving resolution by image registration. CVGIP Graph Model Image Process 1991;53:231–9. https://doi.org/10.1016/1049-9652(91)90045-L.
[23] Elad M, Feuer A. Restoration of a single superresolution image from several blurred, noisy, and undersampled measured images. IEEE Trans Image Process 1997;6:1646–58. https://doi.org/10.1109/83.650118.
[24] Wang Z, Bovik AC, Sheikh HR, Simoncelli EP. Image quality assessment: from error visibility to structural similarity. IEEE Trans Image Process 2004;13:600–12. https://doi.org/10.1109/TIP.2003.819861.
[25] Breuer FA, Blaimer M, Heidemann RM, Mueller MF, Griswold MA, Jakob PM. Controlled aliasing in parallel imaging results in higher acceleration (CAIPIRINHA) for multi-slice imaging. Magn Reson Med 2005;53:684–91. https://doi.org/10.1002/mrm.20401.
[26] Koopmans PJ. Two-dimensional-NGC-SENSE-GRAPPA for fast, ghosting-robust reconstruction of in-plane and slice-accelerated blipped-CAIPI echo planar imaging. Magn Reson Med 2016. https://doi.org/10.1002/mrm.26179.
[27] Noll DC, Nishimura DG, Macovski A. Homodyne detection in magnetic resonance imaging. IEEE Trans Med Imaging 1991;10:154–63. https://doi.org/10.1109/42.79473.
[28] Stemkens B, Sbrizzi A, Andreychenko AA, Crijns SPM, Lagendijk JJW, van den Berg CAT, et al. An optimization framework to maximize signal-to-noise ratio in simultaneous multi-slice body imaging. NMR Biomed 2015. https://doi.org/10.1002/nbm.3457.
[29] Mickevicius NJ, Paulson ES, Muftuler LT, Nencka AS. Application of a k-space interpolating artificial neural network to in-plane accelerated simultaneous multislice. Imaging 2019.
[30] Akçakaya M, Moeller S, Weingärtner S, Uğurbil K. Scan-specific robust artificial-neural-networks for k-space interpolation (RAKI) reconstruction: database-free deep learning for fast imaging. Magn Reson Med 2018. https://doi.org/10.1002/mrm.27420.
[31] Mickevicius NJ, Chen X, Boyd Z, Lee HJ, Ibbott GS, Paulson ES. Simultaneous motion monitoring and truth-in-delivery analysis imaging framework for MR-guided radiotherapy. Phys Med Biol 2018. https://doi.org/10.1088/1361-6560/aaec91.
[32] Feng L, Axel L, Chandarana H, Block KT, Sodickson DK, Otazo R. XD-GRASP: golden-angle radial MRI with reconstruction of extra motion-state dimensions using compressed sensing. Magn Reson Med 2015:1–14. https://doi.org/10.1002/mrm.25665.
[33] Stemkens B, Tijssen RH, de Senneville BD, Heerkens HD, van Vulpen M, Lagendijk JJ, et al. Optimizing 4-dimensional magnetic resonance imaging data sampling for respiratory motion analysis of pancreatic tumors. Int J Radiat Oncol Biol Phys 2015;91:571–8. https://doi.org/10.1016/j.ijrobp.2014.10.050.
[34] Rank CM, Heußer T, Buzan MTA, Wetscherek A, Freitag MT, Dinkel J, et al. 4D respiratory motion-compensated image reconstruction of free-breathing radial MR data with very high undersampling. Magn Reson Med 2017;77:1170–83. https://doi.org/10.1002/mrm.26206.
[35] Mickevicius NJ, Paulson ES. Investigation of undersampling and reconstruction algorithm dependence on respiratory correlated 4D-MRI for online MR-guided radiation therapy. Phys Med Biol 2017;62:2910–21. https://doi.org/10.1088/1361-6560/aa54f2.
[36] Li G, Wei J, Kadbi M, Moody J, Sun A, Zhang S, et al. Novel super-resolution approach to time-resolved volumetric 4-dimensional magnetic resonance imaging with high spatiotemporal resolution for multi-breathing cycle motion assessment. Int J Radiat Oncol 2017;98:454–62. https://doi.org/10.1016/j.ijrobp.2017.02.016.
[37] Freedman JN, Collins DJ, Bainbridge H, Rank CM, Nill S, Kachelrieß M, et al. T2-weighted 4D magnetic resonance imaging for application in magnetic resonance-guided radiotherapy treatment planning. Invest Radiol 2017;52:563–73. https://doi.org/10.1097/RLI.0000000000000381.